

Finite Element Modeling of the Selective Laser Melting Process for Ti-6Al-4V

Alaa Olleak, Zhimin Xi

Department of Industrial and Systems Engineering, Rutgers University, 96 Frelinghuysen Rd,
Piscataway, NJ 08854

Abstract

Physics-based modeling of the selective laser melting (SLM) process is critical for better understanding the influence of the parts quality with respect to various process parameters and scanning strategies. The challenge is to balance model validity, domain size, and computational efficiency so that the model can be practically useful for improving reliability and quality of the printed products. In this paper, a transient thermal finite element model of a SLM process for Ti-6Al-4V is developed using ANSYS for predicting the melt pool size and thermal history. The thermal solution is remapped to the structural problem to predict the induced residual stress of the products. The thermo-mechanical model is capable of handling practical domain size with reasonable computational efficiency on the process level, by developing the re-meshing and remapping technique that adapts with the scanning vector.

1. Introduction

SLM is a common additive manufacturing (AM) process that falls under the category of powder bed fusion process. SLM enables the production of metallic parts that have complex geometry without the need of special tooling and multiple processes in a traditional manufacturing process. Parts manufactured by SLM, however, usually exhibit larger product quality variability than the parts produced by the subtractive methods. In other words, parts quality and reliability control is much more difficult in the SLM, which is mainly caused by different microstructure, induced residual stresses, and manufacturing defects such as high porosity.

Quality of additively manufactured parts was studied by many researchers and porosity was found to be one of the most important factors that affect parts fatigue strength and crack propagation resistance. The porosity takes place due to either excessive energy density that leads to vaporization of the alloy constituents, or insufficient energy density that results in incomplete melting of powder [1]. Residual stresses were also found to be important for parts life, which may be influenced by process parameters, building directions and orientations [2], scanning strategy, and temperature of the powder bed [3]. However, the effects of scanning strategy on the residual stresses are not well understood yet [3]. Furthermore, parts microstructure was also found to be influential in terms of the parts strength and life, and it is affected by process parameters and scanning strategy as well [4]. Although post-processing techniques including heat treatment, and hot isostatic pressing can help alleviate some aforementioned problems, they cannot eliminate them completely such as the porosity which is just reduced to undetectable range [5].

Predicting the part thermal history during SLM is important to understand how the part quality and microstructure are influenced by the process parameters. Numerical methods of the SLM process provide useful tools that help understand temperature distribution and history, induced thermal stresses, and part distortion. Furthermore, they can help optimize the process parameters to achieve better mechanical properties for the printed part as opposed to the expensive and time-consuming experimental approaches.

Several studies were developed to simulate the SLM process using finite element models [6–10]. However, the mesh scheme is still a challenge [11]. On one hand, fine mesh is required to accurately capture the gaussian heat profile and the high temperature gradient at the melt pool. On the other hand, a large domain size is necessary to investigate different scanning strategies on the part level and to develop the layer-by-layer model. Therefore, it is technically challenging to have a high-fidelity model for simulating multiple scanning vectors and scanning strategies. Hence, some studies had to either reduce the domain size or use large element size compared to the laser spot, which may eventually lead to large discretization error. Furthermore, the mesh configuration and attributes are continuously changing because of the newly added layers and changed material states.

Even though the element death and birth approach was found to be useful to model the addition of the layer, this approach requires large number of elements since the element size is restricted by the layer thickness. Although this approach is used in commercial software packages now, it is still computationally expensive for large parts. Another efficient approach is to use adaptive local mesh refinement where the mesh is continuously refined and coarsened according to laser movement [12]. This approach significantly reduces the computational time with acceptable accuracy. However, it needs more time in re-meshing. In addition, remapping is computationally expensive if done frequently. The accumulated errors would result in significant accuracy loss at the high temperature gradient regions. Finally, the thermo-mechanical problem is much more expensive because of the higher degrees of freedom at each node. In addition, re-mapping of the mechanical problem needs equilibrium iterations in order for the structure to reach an equilibrium state.

In this paper, a transient nonlinear finite element model is developed to simulate the SLM process. The objective is to handle a large domain size with high accuracy by considering the thermal properties of the thin powder layer. To reach a compromise between model accuracy and its computational efficiency, adaptive re-meshing is proposed along with the scanning vector. Basically, fine mesh is employed along with the scanning vector to accurately capture the high temperature gradient with minimal re-meshing steps. The model hence should be able to handle large domain size. After the thermal problem, new mesh with larger element size is created, and the temperature information is then mapped to the new mesh for predicting the induced residual stresses in structural analysis. The goal of this study is to predict the temperature distribution and induced residual stresses considering different process conditions and scanning strategies. The model employs Ti-6Al-4V alloy as an example because it is widely used in many applications such as biomedical and aerospace applications in which high reliability and quality are needed. Ti-6Al-4V is a biocompatible material

that has high corrosion resistance, high strength at high temperatures, and high strength to weight ratio.

2. Model Description

2.1 Material modeling

A nonlinear material model was used considering material phase changes and material transitions, i.e., powder melting and solidification. Two temperature-dependent material models were defined for both the powder and solid materials and they behave similarly beyond the melting temperature. The powder thermal conductivity was calculated based on Childs et. al study [13], where the powder thermal conductivity is a function of the thermal conductivity of solid and relative density, equation 1. The volumetric heat capacity for both solid and powder was calculated from the temperature-dependent specific heat and temperature-dependent density. The thermal properties are shown in Fig. 1 and the nonlinear mechanical properties are shown in Fig. 2. It is assumed that mechanical and thermal properties are isotropic. The possible changes in the material properties due to the different process parameters are ignored. For the single bead models, the initial temperature was set as 25 °C. For models including scanning strategies, it is assumed that the powder is preheated to 400 °C [14]. For the mechanical problem, the elastic modulus and thermal expansion are set as the very low values after the melting temperature so that the thermal expansion has negligible effect. The material plasticity model is a temperature-dependent multilinear isotropic hardening from the experimental data in [15].

$$K_p = K_s(T) (1 - 0.2 \varepsilon - 1.73 \varepsilon^2) \quad (1)$$

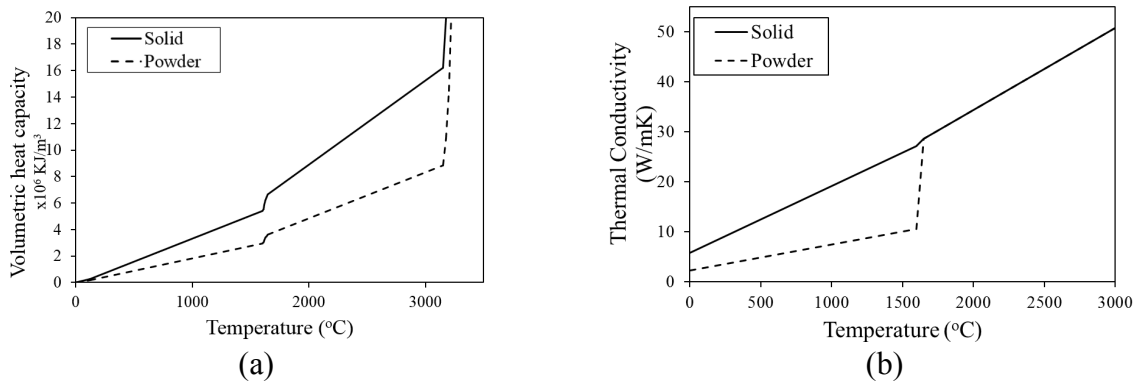


Figure 1: Temperature-dependent properties of Ti6Al4V: (a) Volumetric specific heat, and (b) Thermal conductivity [7, 9]

2.2 Heat source model and boundary conditions

The laser heat flux input is represented by a Gaussian heat source expressed in Eq. 2 [11]. In this study, it is assumed that only the elements on the surface are exposed to the laser beam. The heat flux at any node i with coordinates (x_i, y_i) can be calculated as a function of time as

$$q_i(t) = \frac{2aP}{\pi r_{spot}^2} e^{-2 \frac{(x_i - x_{spot}(t))^2 + (y_i - y_{spot}(t))^2}{r_{spot}^2}} \quad (2)$$

where a is the absorptivity, P is the laser power, and r_{spot} is the beam radius. The equation parameters are shown in Table 1. As will be discussed later, the effect of absorptivity on the results is crucial. Two values are used according to previous simulation in [17] and experimental results in [18]. Convection at the surface is allowed assuming that the surrounding gas is Argon ($h=10 \text{ W/m}^2\text{K}$). Since the part size is large, the mild steel plate is not included in the model.

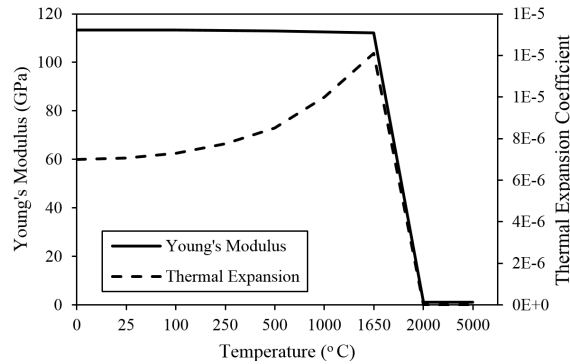


Figure 2: Temperature dependent mechanical properties of Ti-6Al-4V

2.3 Mesh configuration

Accurate representations of the heat source and the melt pool dimension require a small element size in the finite element model. Representing the entire domain using small element size, however, is computationally prohibitive especially for models considering multiple scanning vectors. Therefore, 8-noded hexahedron elements with edge size of $10 \mu\text{m}$ were used to represent the powder and melt pool region. For the rest of the domain where the temperature gradient is not high, free 4-noded tetrahedral elements were used. For these elements, the material assignment was kept as solid. This is valid on the ground that powder thermal conductivity below the melting temperature is low and the heat flux perpendicular to the laser beam direction is low as well. Fig.3 shows the mesh configuration for a 2 mm scan length with single bead analysis.

Table 1: Process parameters used in the model

Power (Watt)	100,150, and 195
Scanning speeds (mm/s)	500, 750, 1000, 1200
Absorptivity (a)	0.4, 0.6
Spot diameter	$100 \mu\text{m}$
Layer thickness	$30 \mu\text{m}$

Having such small element size allows us to take the powder's thermal properties into consideration. Therefore, re-meshing is needed to keep assigning small element size where the temperature gradient is high and assigning large element size for the remaining part. A typical mesh configurations for a large part ($6\text{mm} \times 6\text{mm} \times 1\text{mm}$) for

both bidirectional and chessboard scanning strategies are shown in Fig. 4. The mesh near the surface always have small size to keep the temperature re-mapping accurate. In the shown mesh in Fig. 4, the size of elements on the top size does not exceed 50 μm .

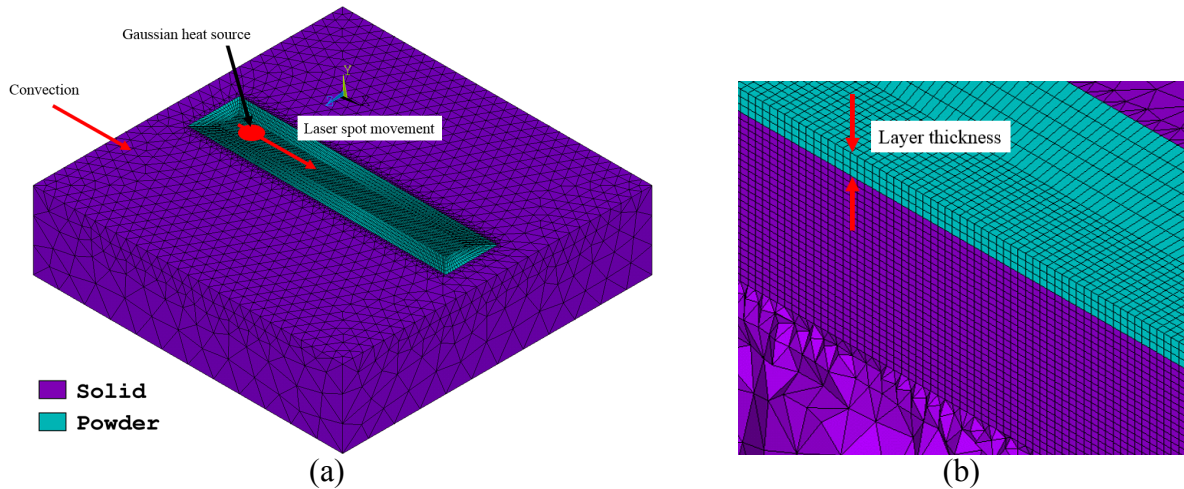


Figure 3: Mesh configuration for single bead model: (a) Block size 3 mm \times 3 mm \times 0.75 mm, and (b) cross sectional image showing mesh density at melt pool region

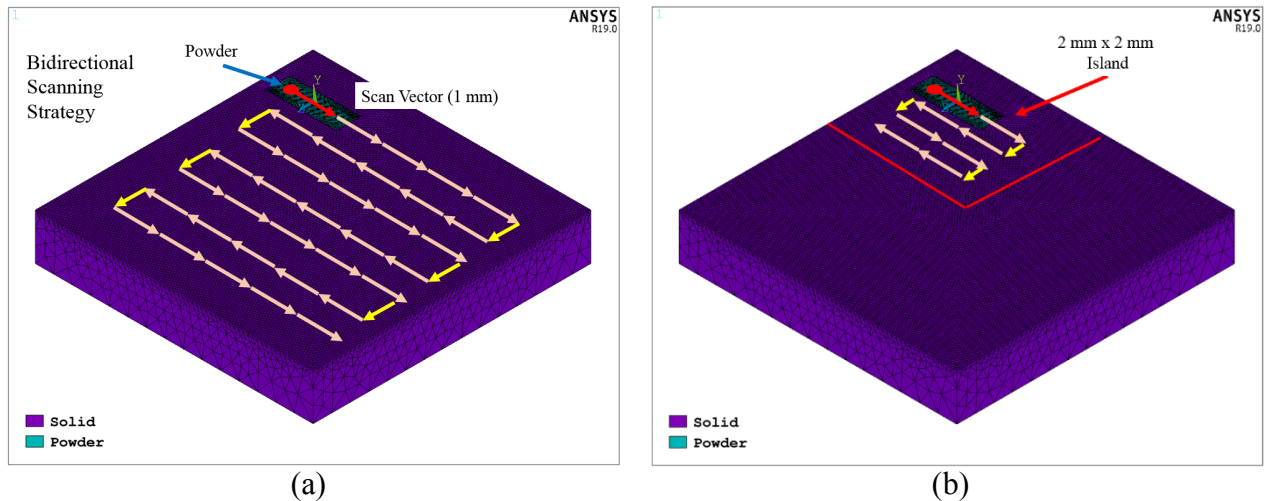


Figure 4: Mesh configuration for large block size 6 mm \times 6 mm \times 1 mm: (a) Bidirectional scanning strategy, and (b) Chessboard scanning strategy (Island size: 2 mm \times 2 mm).

2.4 Analysis

The analysis is transient in both thermal and mechanical problems. For the thermal problem, the laser location is updated after each time step, which is the time needed for the laser moving 10 μm (i.e., the element edge length). The phase change and temperature dependent properties as shown in Fig. 1 add high nonlinearity to the problem, which requires the full Newton Raphson method. To ensure convergence, the automatic time stepping was turned on in ANSYS. Once the temperature information from the scanning vector is calculated, new mesh is generated, and remapping is

followed to calculate the initial temperature of the new mesh. The thermal solution is calculated from the governing equation shown in Eq. (3).

$$\rho C_p \frac{\delta T}{\delta t} = k \left[\frac{\delta T^2}{\delta x^2} + \frac{\delta T^2}{\delta y^2} + \frac{\delta T^2}{\delta z^2} \right] + Q \quad (3)$$

where ρ is the density, C_p is the specific heat capacity, t is the time, T is the temperature, k is the thermal conductivity, and Q is the heat input per unit volume.

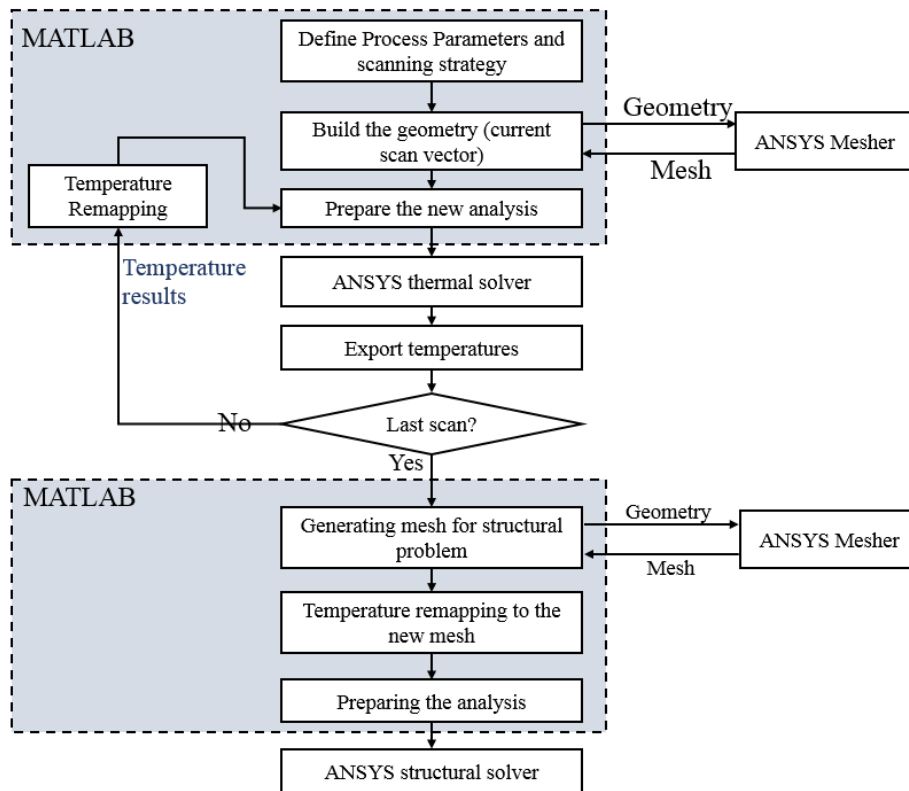


Figure 5: Methodology flow diagram

The mechanical problem would be too expensive to solve if keeps the same mesh from the thermal problem with a large stiffness matrix. Therefore, coarse and uniform mesh was preferable. Brick elements with 8 nodes were used for the structural analysis. The nodal temperature as a function of time was calculated from the thermal analysis results and applied to the node as a body force. The last step of the structural problem is a relaxation step where all the body forces are removed, and the part residual stresses are estimated at the room temperature.

Remapping the node temperature from old mesh to new mesh requires locating the nodes from the new mesh in the old mesh, finding the corresponding elements, and then performing element interpolation. However, this process was found to be time consuming. Therefore, a simple weighting function formulated in Eq. (4), was used for the remapping. The nearest 4 nodes from the solved problem were taken into consideration for calculating the nodal temperature at the new mesh.

$$T_i(t) = \begin{cases} T_j & d_j \leq 2.5 \mu m \\ \frac{\sum_{j \in N} \frac{T_j(t)}{d_j}}{\sum_{k \in N} \frac{1}{d_k}} & d_j > 2.5 \mu m \end{cases} \quad (4)$$

where N represents the nearest 4 nodes to node i , T_j is the temperature of node j in old mesh, and d_j is the distance from node j in old mesh to node i in the new mesh. The overall analysis flowchart is shown in Fig. 5 with a seamless integration between MATLAB and ANSYS. An example of the re-mapping result is shown in Fig. 6, in which good degree of agreement is maintained while greatly improving the computational efficiency.

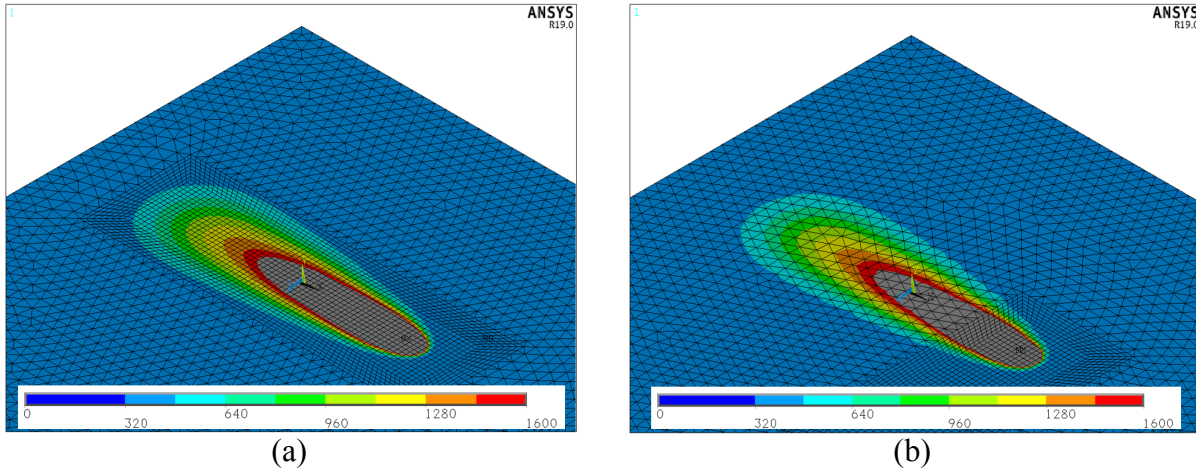


Figure 6: Temperature remapping Results between different scanning vectors: (a) before remeshing, and (b) after remeshing

3. Model Results

The single bead model results are compared to the experimental results in [19]. Overall, the melt pool width shows acceptable agreement with the experimental results. However, the melt pool depth was underestimated. Fig. 7 shows the temperature distribution of a scanning vector using 150 W laser power with 1200 mm/s scanning speed.

The effect of the scanning speed and power are compared to the experimental results in [12,13]. The melt pool width shows acceptable agreement with the experimental results as shown in Fig. 8. Like the experimental observations, the predicted melt pool width has an increasing trend with the scanning speed and laser power. Though the predicted melt pool depth is underestimated compared to experimental results, the penetration depth increases when power increases and scanning speed reduces. This deviation of the melt pool depth predictions could be due to the simplification of the heat source model by including only the element on the top surface or ignoring the stochastic nature of the process. Furthermore, the randomly distributed powder particles and their size could affect the powder thermal conductivity and their absorptivity as well.

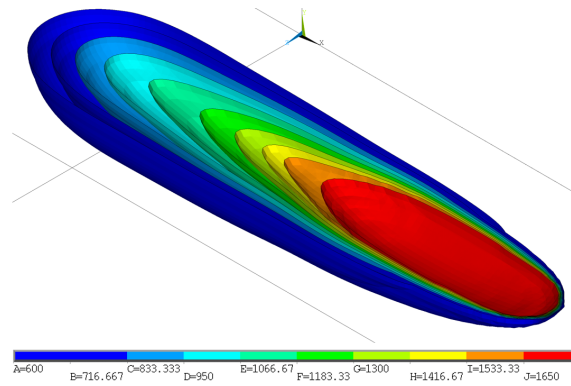


Figure 7: Temperature distribution for $P=150$ Watt, and $V=1200$ mm/s.

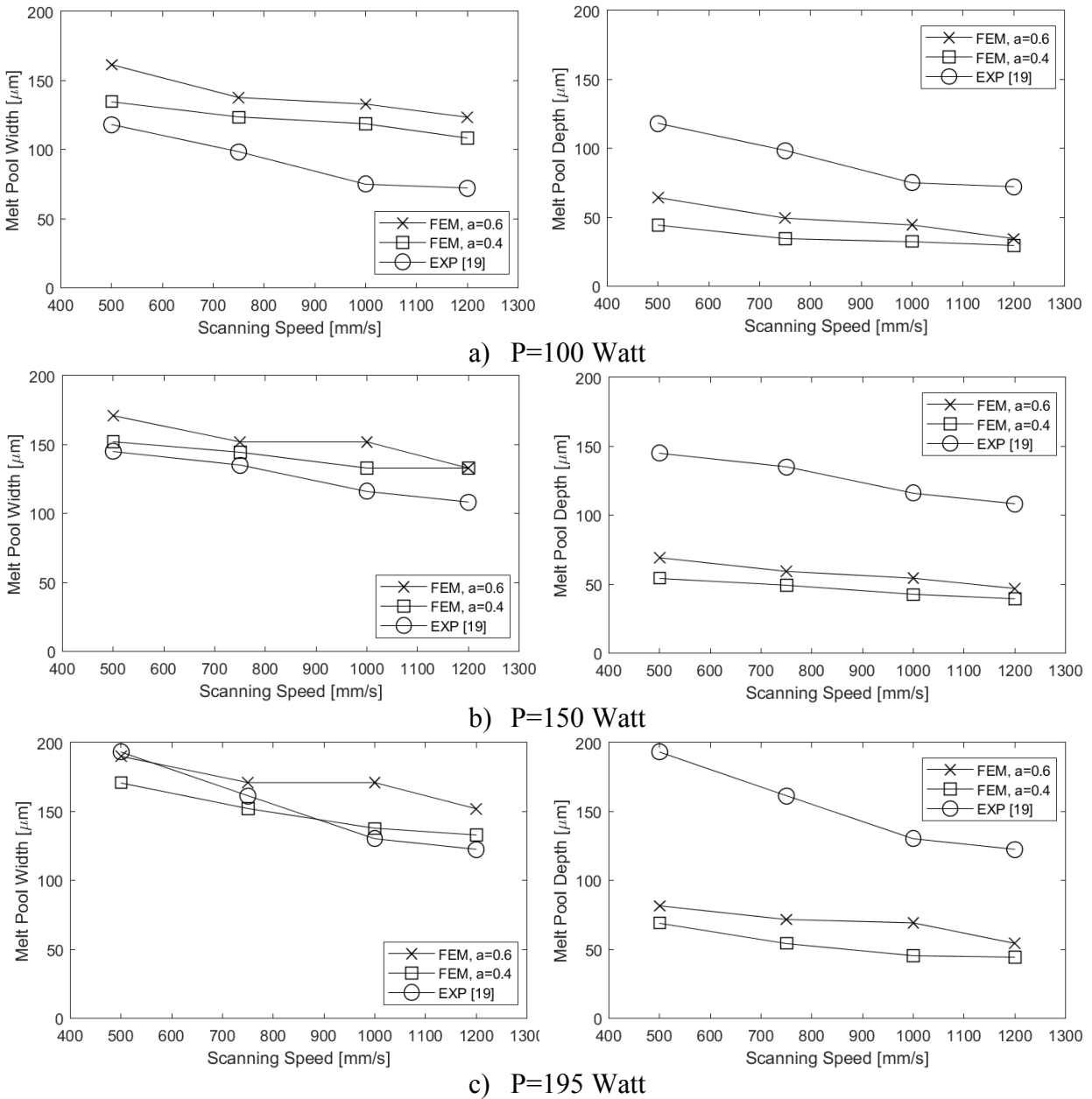


Figure 8: Thermal results of single bead analysis for different process conditions

The model was extended to a larger case where a bidirectional and chessboard scanning strategies were adopted. A block size of $6\text{ mm} \times 6\text{ mm} \times 1\text{ mm}$ was considered with hatch spacing of 0.1 mm . The scanning pattern for the bidirectional was shown in Fig. 4(a). The temperature distribution and the melt pool size for the bidirectional and the chessboard scanning strategies are shown in Fig. 9 and Fig. 10, respectively. For both scanning strategies, the melt pool size is influenced by the temperature distribution from the previous scanning vector. It was observed that the melt pool width and depth during the second scan are larger than the one in the first scan. The predicted residual stresses for the bidirectional scanning strategy are shown in Fig. 11. Within depth $100\text{ }\mu\text{m}$, it was found that the principal component of residual stresses is $108\pm 47\text{ MPa}$. This result can find an agreement with the measured residual stresses for similar scanning strategy and process parameter in [3]. Although using coarser mesh for the structural analysis is computationally efficient, a fine mesh at high temperature gradient regions is needed to allow capturing that temperature variation.

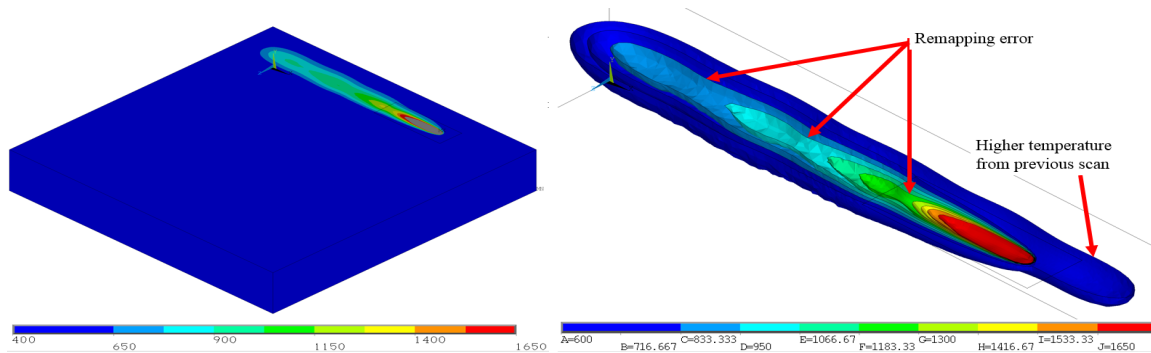


Figure 9: Temperature distribution for bidirectional scanning strategy for a large block ($6\text{ mm} \times 6\text{ mm} \times 1\text{ mm}$) ($P=200\text{ W}$, $V=650\text{ mm/s}$)

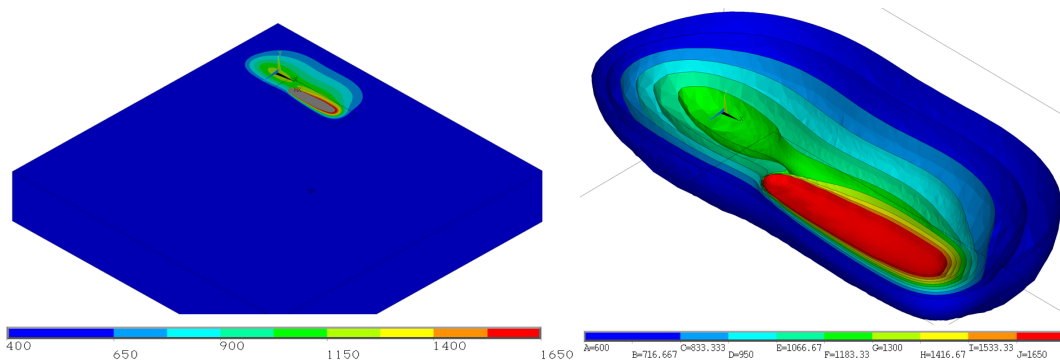


Figure 10: Temperature distribution for chessboard scanning strategy for a large block ($6\text{ mm} \times 6\text{ mm} \times 1\text{ mm}$) and 2 mm chessboard block length ($P=200\text{ Watt}$, $V=1000\text{ mm/s}$)

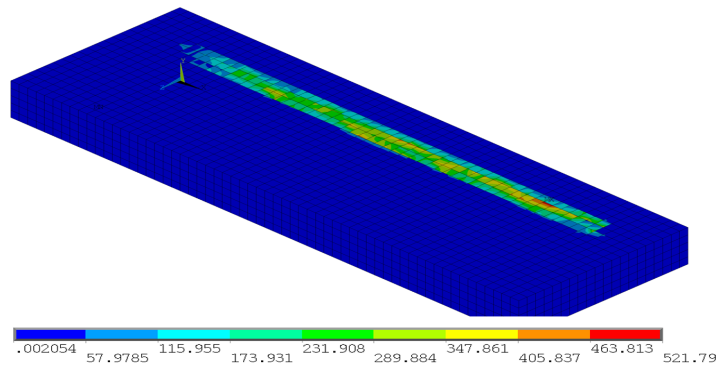


Figure 11: Induced residual stresses (principal component) after bidirectional scanning strategy

4. Conclusion and Future Work

This paper proposes a thermo-mechanical model for modeling the SLM process for Ti-6Al-4V using the re-meshing technique that adapts with different scanning strategies. As compared to available experimental results, the model exhibits reasonable accuracy and is also capable of handling large domain size with relatively high computational efficiency. The model predicts the melt pool width accurately but underestimates the melt pool depth given available experimental data. The reason could come from the model assumptions and simplifications. Hence, a systematic model validation study will be followed after this study. In addition, various uncertainties in model process parameters may greatly affect the thermal and mechanical properties of the printed products. Hence, these influences will be studied as well especially from the reliability and quality perspective.

5. Acknowledgement

Authors appreciate research funding support from DARPA – Young Faculty Award and ANSYS for providing software for running the simulation.

6. References

- [1] H. Gong, K. Rafi, H. Gu, T. Starr, and B. Stucker, “Analysis of defect generation in Ti-6Al-4V parts made using powder bed fusion additive manufacturing processes,” *Addit. Manuf.*, vol. 1–4, pp. 87–98, Oct. 2014.
- [2] P. Edwards and M. Ramulu, “Fatigue performance evaluation of selective laser melted Ti-6Al-4V,” *Mater. Sci. Eng. A*, vol. 598, pp. 327–337, 2014.
- [3] H. Ali, H. Ghadbeigi, and K. Mumtaz, “Effect of scanning strategies on residual stress and mechanical properties of Selective Laser Melted Ti6Al4V,” *Mater. Sci. Eng. A*, vol. 712, pp. 175–187, Jan. 2018.
- [4] X. Zhao *et al.*, “Comparison of the microstructures and mechanical properties of Ti-6Al-4V fabricated by selective laser melting and electron beam melting,” *Mater. Des.*, vol. 95, pp. 21–31, 2016.
- [5] S. Leuders *et al.*, “On the mechanical behaviour of titanium alloy TiAl6V4 manufactured by selective laser melting: Fatigue resistance and crack growth performance,” *Int. J. Fatigue*, vol. 48, pp. 300–307, 2013.
- [6] C. H. Fu and Y. B. Guo, “Three-Dimensional Temperature Gradient Mechanism in Selective Laser Melting of Ti-6Al-4V,” *J. Manuf. Sci. Eng.*, vol. 136, no. 6, p. 061004,

- 2014.
- [7] C. Teng *et al.*, “Simulating Melt Pool Shape and Lack of Fusion Porosity for Selective Laser Melting of Cobalt Chromium Components,” *J. Manuf. Sci. Eng.*, vol. 139, no. 1, p. 011009, 2016.
 - [8] L. Li, C. Lough, A. Replogle, D. Bristow, R. Landers, and E. Kinzel, “Thermal Modeling of 304L Stainless Steel Selective Laser Melting,” *Solid Free. Fabr.*, vol. 6061, pp. 1068–1081, 2017.
 - [9] S. Lynch, “Melt Pool Evolution Study in Selective Laser Melting,” *Dyn. Syst. with Appl. using MATLAB*, vol. 53, pp. 1182–1194, 2013.
 - [10] I. A. Roberts, C. J. Wang, R. Esterlein, M. Stanford, and D. J. Mynors, “A three-dimensional finite element analysis of the temperature field during laser melting of metal powders in additive layer manufacturing,” *Int. J. Mach. Tools Manuf.*, vol. 49, no. 12–13, pp. 916–923, 2009.
 - [11] Z. Luo and Y. Zhao, “A survey of finite element analysis of temperature and thermal stress fields in powder bed fusion Additive Manufacturing,” *Addit. Manuf.*, vol. 21, pp. 318–332, May 2018.
 - [12] D. Pal *et al.*, “A Generalized Feed-Forward Dynamic Adaptive Mesh Refinement and Derefinement Finite-Element Framework for Metal Laser Sintering—Part II: Nonlinear Thermal Simulations and Validations ²,” *J. Manuf. Sci. Eng.*, vol. 138, no. 6, p. 061003, 2016.
 - [13] T. H. C. Childs, M. Berzins, G. R. Ryder, and A. Tontowi, “Selective laser sintering of an amorphous polymer—simulations and experiments,” *Proc. Inst. Mech. Eng. Part B J. Eng. Manuf.*, vol. 213, no. 4, pp. 333–349, 1999.
 - [14] H. Ali, L. Ma, H. Ghadbeigi, and K. Mumtaz, “In-situ residual stress reduction, martensitic decomposition and mechanical properties enhancement through high temperature powder bed pre-heating of Selective Laser Melted Ti6Al4V,” *Mater. Sci. Eng. A*, vol. 695, no. February, pp. 211–220, 2017.
 - [15] W.-S. Lee and C.-F. Lin, “High-temperature deformation behaviour of Ti6Al4V alloy evaluated by high strain-rate compression tests,” *J. Mater. Process. Technol.*, vol. 75, no. 1–3, pp. 127–136, 1998.
 - [16] M. Boivineau *et al.*, “Thermophysical properties of solid and liquid Ti-6Al-4V (TA6V) alloy,” *Int. J. Thermophys.*, vol. 27, no. 2, pp. 507–529, 2006.
 - [17] K. Zeng, D. Pal, and B. E. Stucker, “A Review of Thermal Analysis Methods in Laser Sintering and Selective Laser Melting,” *Proc. Solid Free. Fabr. Symp.*, pp. 796–814, 2012.
 - [18] S. A. Khairallah, A. T. Anderson, A. Rubenchik, and W. E. King, “Laser powder-bed fusion additive manufacturing: Physics of complex melt flow and formation mechanisms of pores, spatter, and denudation zones,” *Acta Mater.*, vol. 108, pp. 36–45, Apr. 2016.
 - [19] J. J. S. Dilip *et al.*, “Influence of processing parameters on the evolution of melt pool, porosity, and microstructures in Ti-6Al-4V alloy parts fabricated by selective laser melting,” *Prog. Addit. Manuf.*, no. August, 2017.
 - [20] H. Gong, D. Christiansen, J. Beuth, and J. J. Lewandowski, “Melt Pool Characterization for Selective Laser Melting of Ti-6Al-4V Pre-alloyed Powder,” *Solid Free. Fabr. Symp.*, pp. 256–267, 2014.